Editors' Suggestion

Multinucleon transfer mechanism in ^{250}Cf + ^{232}Th collisions using the quantal transport description based on the stochastic mean-field approach

S. Ayik [1,*] M. Arik [2] O. Yilmaz [2] B. Yilmaz [3] and A. S. Umar [4]

[1]*Physics Department, Tennessee Technological University, Cookeville, Tennessee 38505, USA*
[2]*Physics Department, Middle East Technical University, 06800 Ankara, Turkey*
[3]*Physics Department, Faculty of Sciences, Ankara University, 06100 Ankara, Turkey*
[4]*Department of Physics and Astronomy, Vanderbilt University, Nashville, Tennessee 37235, USA*

(Received 19 October 2022; accepted 1 December 2022; published 10 January 2023)

Production cross sections of heavy neutron-rich isotopes are calculated by employing quantal transport description in ^{250}Cf + ^{232}Th collisions. This quantal transport description is based on the stochastic mean-field approach, and it provides a microscopic approach beyond time-dependent Hartree-Fock theory to include mean-field fluctuations. Deexcitation of primary fragments is determined by employing the statistical GEMINI++ code. Calculations provide predictions for production cross sections of neutron rich transfermium isotopes without any adjustable parameters.

DOI: 10.1103/PhysRevC.107.014609

I. INTRODUCTION

In recent years extensive experimental and theoretical investigations have been carried out for the production of heavy elements close to the superheavy island with proton numbers $Z > 100$ [1–16]. Fusion reactions are a natural mechanism for the production of very heavy nuclei. Superheavy elements are identified by following the decay pattern of the primary heavy fusion product. Thus far super heavy elements have been synthesized either in cold fusion reactions [17] or in hot fusion reactions [14,18], using actinide nuclei. Highly excited compound nuclei deexcite mostly by neutron emission and secondary fission. As a result, fusion reactions may not be the most efficient way to produce neutron rich heavy isotopes.

As an alternative mechanism, for the production of neutron rich heavy isotopes, multinucleon transfer (MNT) processes have been experimentally investigated with actinide targets near barrier energies, and more investigations are currently in progress. Such investigations may provide a more efficient mechanism for the production of heavy neutron rich isotopes. The multinucleon transfer mechanism has been investigated using several phenomenological approaches including the multidimensional Langevin model [19–25], dinuclear system model [26–28], and quantum molecular dynamics model [29–31]. In order to provide more accurate description of collision dynamics and for the MNT mechanism it is important to develop microscopic approaches, which also provide a test for phenomenological models. Time-dependent Hartree-Fock (TDHF) theory provides a microscopic description for the mean evolution of collective dynamics at low bombarding energies [32–41]. However, the TDHF theory has a severe limitation: it can only describe the most probable dynamical path of the collision dynamics with small fluctuations around it. It describes mean kinetic energy loss due to one body dissipation rather well, but it cannot describe the large dispersions of mass and charge distribution of the fragments. To remedy this problem one must go beyond TDHF [42–45]. The time-dependent random phase approximation of Balian and Vénéroni provides an important improvement of the mean-field description. This approach has been applied for analysis of multinucleon transfer in several studies [46–50]. However, the approach is limited to calculating dispersions of charge and mass distributions in symmetric collisions.

The stochastic mean-field (SMF) approach provides a further improvement of the TDHF theory beyond the mean-field approximation [45,51], and can be applied to asymmetric collisions. In Sec. II we present results of TDHF calculations for the collisions of the ^{250}Cf + ^{232}Th system at $E_{\text{c.m.}} = 950$ MeV. In Sec. III, we briefly describe the quantal transport description of multinucleon transfer based on the SMF approach. We present an analysis of multinucleon transfer mechanism for the same reaction. This analysis is essentially a complementary description of the work of Kedziora and Simenel [52], in which the multinucleon transfer mechanism has been investigated in the TDHF approximation alone. In Sec. IV, we present results of quantal transport description based on the SMF approach for the ^{250}Cf + ^{232}Th reaction. Our calculations can describe primary and secondary isotope production cross sections including mean values and fluctuations without any adjustable parameters except standard parameters of the Skyrme energy density functional. In Sec. V, conclusions are given.

II. MEAN-FIELD DESCRIPTION

The microscopic TDHF theory, employing effective Skyrme type energy density functionals, has been used

*ayik@tntech.edu

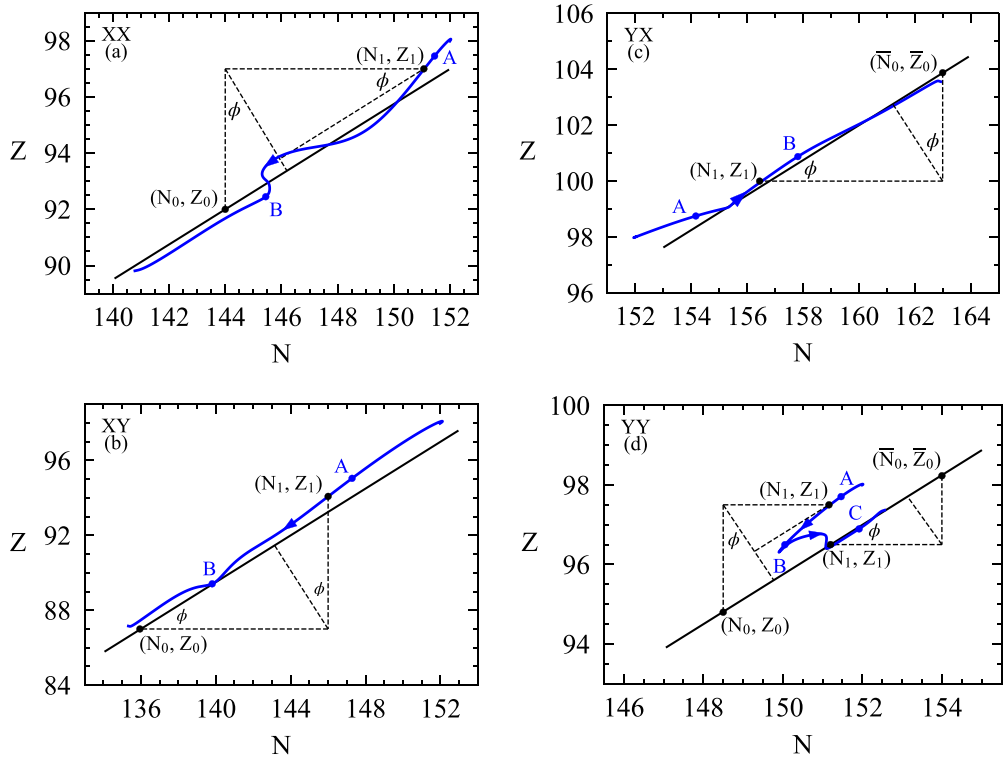

FIG. 1. Blue curves show the drift path of Cf-like fragments in the head-on collision of the $^{250}\mathrm{Cf} + ^{232}\mathrm{Th}$ system at $E_{\mathrm{c.m.}} = 950$ MeV in tip-tip (XX), tip-side (XY), side-tip (YX), and side-side (YY) geometries. Labels A, B, and C indicate intervals used in determining the average values of the reduced isoscalar curvature parameter β in Eqs. (9)–(11).

extensively for describing heavy-ion collisions and nuclear fusion [32–36,39–41]. The mean-field theory provides a good description for the most probable dynamical path of the collective motion at low energy heavy-ion collisions, including the one body dissipation mechanism. The TDHF is a deterministic approach for many body dynamics in the sense that mean-field evolution starting with a given initial condition leads to a single, deterministic final state. For example, for a collision with a given charge and mass asymmetry it leads to a single exit channel with a certain charge and mass asymmetry.

In the $^{250}\mathrm{Cf} + ^{232}\mathrm{Th}$ system, both projectile and target nuclei exhibit strong prolate deformation in their ground states. As a result, the collision dynamics and multinucleon transfer mechanism strongly depend on the collision geometry. We consider four different initial collision geometries at the same bombarding energy $E_{\mathrm{c.m.}} = 950$ MeV. In analogy with the work of Kedziora and Simenel of Ref. [52], we indicate initial orientation of the target or projectile along the beam direction with letter X, and perpendicular to the beam direction with letter Y. Four different collision geometries are represented as XX, XY, YX, and YY and correspond to tip-tip, tip-side, side-tip, and side-side geometries, respectively (see Figs. 2 and 3 of Ref. [52]). Based on the work of Ref. [52], it is expected that the YZ collision geometry will give similar results as the YY orientation. As a result, we did not include the YZ geometry in our calculations. As a convention, the first letter indicates the initially heavy partner of the colliding system. Table I exhibits results of TDHF calculations for different values of initial orbital angular momentum ℓ_i, final values of mass and charge numbers of Cf-like A_1^f and Z_1^f and Th-like A_2^f and Z_2^f fragments, final total kinetic energy (TKE), total excitation energy (E^*), and scattering angles in the center of mass frame $\theta_{\mathrm{c.m.}}$ and laboratory frame θ_1^{lab} and θ_2^{lab} for the four different collision geometries. The table also includes asymptotic values of neutron dispersion $\sigma_{NN}(\ell)$, proton dispersion $\sigma_{ZZ}(\ell)$, mixed dispersions $\sigma_{NZ}(\ell)$, and mass dispersion $\sigma_{AA}(\ell) = \sqrt{\sigma_{NN}^2(\ell) + \sigma_{ZZ}^2(\ell) + \sigma_{NZ}^2(\ell)}$, for each orbital angular momentum. These dispersions are defined as $\sigma_{NN}^2(\ell) = \overline{\delta N^\lambda \delta N^\lambda}$, $\sigma_{ZZ}^2(\ell) = \overline{\delta Z^\lambda \delta Z^\lambda}$, and $\sigma_{NZ}^2(\ell) = \overline{\delta N^\lambda \delta Z^\lambda}$. In the quantities the bar indicates ensemble averages of the product of fluctuating neutron δN^λ and proton δZ^λ numbers, which are discussed in Sec. IV A. To reduce the computation time, we have chosen the initial orbital angular momentum in steps of $40\hbar$. The calculations presented in the rest of the paper employed the TDHF code [53,54] using the SLy4d Skyrme energy density functional [55], with a box size of $60 \times 60 \times 36$ fm in the x-y-z directions, respectively.

As seen from Table I, distinct geometries result in different nucleon transfer mechanisms. The different nucleon transfer mechanisms for head-on collisions are observed more clearly from the time evolution of neutron $N(t)$ and proton $Z(t)$ numbers of Cf-like fragments or Th-like fragments. In Fig. 8 of the Appendix, we plot the time evolution of neutron and proton numbers for the Cf-like fragments for the four different geometries studied. In standard TDHF calculations, time

TABLE I. Results of the TDHF and SMF calculations for the ^{250}Cf + ^{232}Th system at $E_{\text{c.m.}} = 950$ MeV in tip-tip (XX), tip-side (XY), side-tip (YX), and side-side (YY) geometries.

Geometry	ℓ_i ($\hbar$)	Z_1^f	A_1^f	Z_2^f	A_2^f	ℓ_f ($\hbar$)	TKE	E^*	σ_{NN}	σ_{ZZ}	σ_{NZ}	σ_{AA}	$\theta_{\text{c.m.}}$	θ_1^{lab}	θ_2^{lab}
XX	0	89.9	230.7	98.1	251.3	0.0	612.8	335.9	8.6	5.5	5.5	13.6	180.0	0.0	0.0
	40	90.7	232.7	97.3	249.3	27.1	606.7	342.6	8.6	5.6	5.6	13.7	171.9	3.7	28.6
	80	92.9	238.4	95.1	243.6	63.1	603.9	345.4	8.7	5.7	5.7	13.9	163.2	7.6	47.6
	120	95.9	246.5	92.1	235.5	92.4	589.0	362.6	8.8	5.7	5.7	14.0	154.0	11.5	55.9
	160	98.6	253.3	89.4	228.7	123.3	571.1	375.8	8.9	5.8	5.8	14.1	144.5	15.3	57.8
	200	98.9	253.9	89.1	228.1	147.9	564.3	381.4	8.8	5.7	5.7	14.1	135.2	19.1	56.0
	240	98.3	252.7	89.7	229.3	178.1	563.6	384.1	8.8	5.7	5.7	14.0	125.3	23.3	53.1
	280	96.9	248.9	91.1	233.0	219.5	567.0	382.3	8.7	5.6	5.6	13.8	115.3	27.8	49.3
	320	97.2	249.7	90.8	232.3	243.4	590.4	358.8	8.4	5.5	5.5	13.4	106.9	31.6	47.1
	360	97.5	250.0	90.5	232.0	258.7	625.5	324.5	8.0	5.2	5.2	12.7	100.9	34.7	45.8
	400	96.6	247.5	91.4	234.4	283.8	668.3	279.9	7.4	4.8	4.8	11.6	95.8	37.8	44.4
	440	96.7	248.4	91.3	233.6	330.9	718.7	229.5	6.6	4.3	4.3	10.3	90.5	41.0	43.2
	480	97.2	249.1	90.8	232.9	398.7	774.9	174.4	5.6	3.7	3.7	8.5	85.7	44.1	42.0
XY	0	87.1	222.4	100.9	259.6	0.0	627.4	316.3	7.8	5.2	5.8	12.4	180.0	0.0	0.0
	40	87.5	223.5	100.5	258.5	30.7	624.7	322.7	7.8	5.2	5.8	12.4	169.7	4.9	31.3
	80	88.7	227.0	99.3	255.0	64.7	625.0	321.8	7.8	5.2	5.8	12.4	159.1	9.9	47.7
	120	90.3	231.4	97.7	250.6	98.6	612.5	336.2	7.8	5.2	5.8	12.5	148.4	14.6	52.9
	160	91.6	235.1	96.4	246.9	141.6	592.2	358.0	7.9	5.2	5.8	12.5	137.1	19.5	52.7
	200	93.2	239.1	94.8	242.9	181.7	586.2	364.0	7.9	5.2	5.8	12.5	125.9	24.2	51.3
	240	93.9	241.3	94.1	240.7	212.1	591.6	359.1	7.8	5.2	5.8	12.4	116.4	28.2	49.1
	280	95.4	245.0	92.6	237.0	244.7	569.0	380.9	7.7	5.1	5.7	12.2	107.6	31.3	46.0
	320	96.3	247.4	91.7	234.6	258.7	607.0	343.2	7.4	4.9	5.4	11.7	102.1	34.1	45.4
	360	96.8	248.2	91.2	233.8	286.5	634.0	314.2	7.1	4.8	5.1	11.2	96.1	37.0	43.8
	400	97.3	249.6	90.7	232.4	316.7	667.6	280.1	6.8	4.5	4.8	10.6	91.4	39.4	42.7
	440	97.3	249.7	90.7	232.3	363.7	708.3	239.4	6.3	4.2	4.4	9.8	87.4	42.0	41.7
	480	97.8	251.3	90.2	230.7	400.7	745.3	203.4	5.7	3.8	3.8	8.7	83.5	44.2	40.7
YX	0	103.5	266.5	84.5	215.5	0.0	647.7	297.1	7.6	5.1	5.4	11.9	180.0	0.0	0.0
	40	103.6	266.7	84.4	215.3	30.8	647.3	296.4	7.6	5.1	5.4	11.9	169.9	4.4	70.0
	80	103.4	266.3	84.6	215.7	73.4	644.5	298.2	7.6	5.1	5.4	12.0	159.6	8.9	71.7
	120	103.2	265.3	84.8	216.7	96.8	632.4	311.6	7.6	5.1	5.4	12.0	149.6	13.1	68.0
	160	102.5	263.4	85.5	218.6	133.0	613.8	330.9	7.6	5.2	5.5	12.0	139.1	17.5	62.8
	200	101.4	260.5	86.6	221.5	177.4	607.1	336.6	7.6	5.2	5.5	12.0	128.6	22.0	58.1
	240	100.4	257.3	87.6	224.7	207.5	601.3	344.8	7.6	5.1	5.5	12.0	119.0	26.1	53.5
	280	99.0	253.6	89.0	228.4	238.9	597.5	348.2	7.6	5.1	5.4	11.9	110.1	30.1	49.2
	320	97.2	249.9	90.8	232.1	265.0	615.7	332.0	7.4	5.0	5.2	11.6	103.1	33.6	46.4
	360	96.5	248.6	91.5	233.4	286.2	642.3	307.0	7.1	4.8	5.0	11.2	97.6	36.4	44.7
	400	96.2	247.5	91.8	234.5	315.1	668.2	282.9	6.8	4.7	4.7	10.6	92.3	39.3	42.8
	440	96.1	247.2	91.9	234.8	346.4	700.5	249.7	6.4	4.4	4.3	9.9	87.9	41.9	41.5
	480	96.1	247.2	91.9	234.8	387.8	740.5	209.7	5.9	4.0	3.8	8.9	84.2	44.3	40.5
YY	0	97.4	250.0	90.6	232.0	0.0	620.0	327.7	9.3	6.1	6.8	14.7	180.0	0.0	0.0
	40	98.2	252.2	89.8	229.8	27.3	634.6	315.2	9.3	6.1	6.8	14.7	167.6	5.5	55.3
	80	97.8	251.5	90.2	230.5	51.1	632.9	316.8	9.2	6.0	6.8	14.6	155.0	11.2	62.1
	120	97.5	251.1	90.5	230.9	90.9	627.0	321.7	9.2	6.0	6.7	14.5	142.8	16.5	60.6
	160	96.8	248.9	91.2	233.1	135.7	613.6	335.7	9.1	6.0	6.7	14.4	130.7	21.8	56.2
	200	96.7	248.3	91.3	233.7	177.0	616.9	331.3	8.9	5.8	6.5	14.1	120.7	26.3	52.9
	240	97.2	249.7	90.8	232.3	199.3	639.5	308.2	8.6	5.7	6.2	13.6	113.1	29.8	51.2
	280	97.0	249.0	91.0	233.0	236.8	638.0	311.3	0.0	5.5	6.0	13.2	105.1	33.2	47.7
	320	97.4	249.8	90.6	232.2	280.7	627.6	320.1	8.2	5.4	5.8	12.8	97.5	36.1	44.4
	360	97.6	250.3	90.4	231.7	312.6	638.7	310.6	7.8	5.1	5.5	12.1	93.0	38.1	42.8
	400	97.5	250.4	90.5	231.6	341.0	659.1	290.9	7.3	4.8	5.1	11.3	87.5	40.8	40.8
	440	97.5	250.5	90.5	231.5	378.4	687.9	260.8	6.8	4.5	4.6	10.5	83.8	42.9	39.7
	480	97.4	250.3	90.6	231.7	416.4	725.6	222.1	6.3	4.2	4.0	9.4	81.2	44.9	39.2

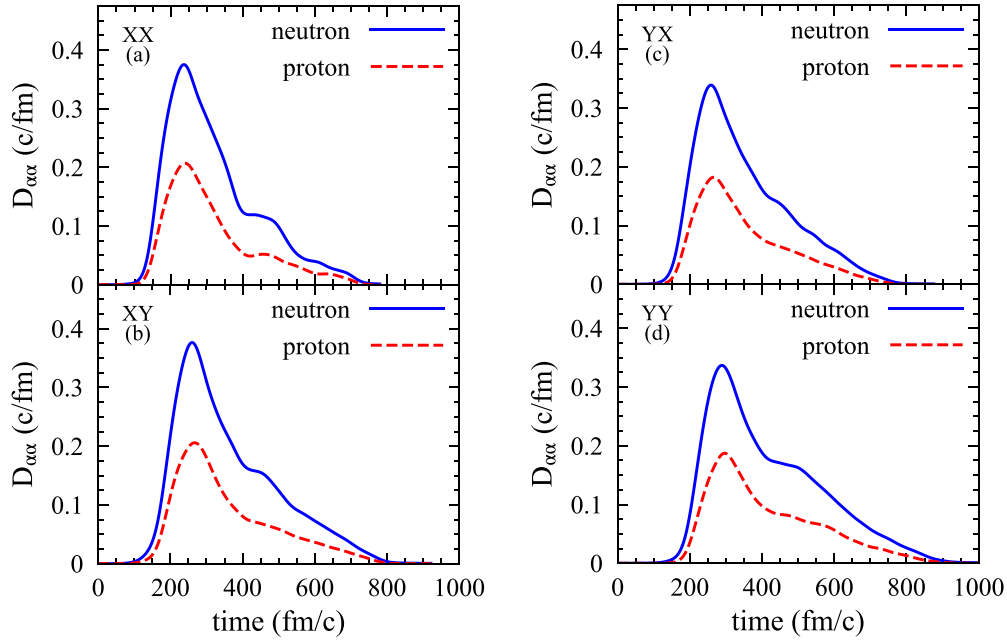

FIG. 2. Neutron and proton diffusion coefficient in the head-on collision of the ^{250}Cf + ^{232}Th system at $E_{\text{c.m.}} = 950$ MeV in tip-tip (XX), tip-side (XY), side-tip (YX), and side-side (YY) collision geometries.

evolutions of macroscopic variables for a dinuclear complex, such as the charge and mass of targetlike or projectilelike fragments, are not utilized explicitly. Often just the values of macroscopic variables at the exit channel are employed in the analysis of the reaction mechanism. Drift paths, which show the evolution of the system in the N-Z plane, carry more detailed information about the nucleon transfer mechanisms. As a result of shell effects on dynamics, drift paths exhibit different behavior in different collision geometries and include detailed information of time evolution of the mean

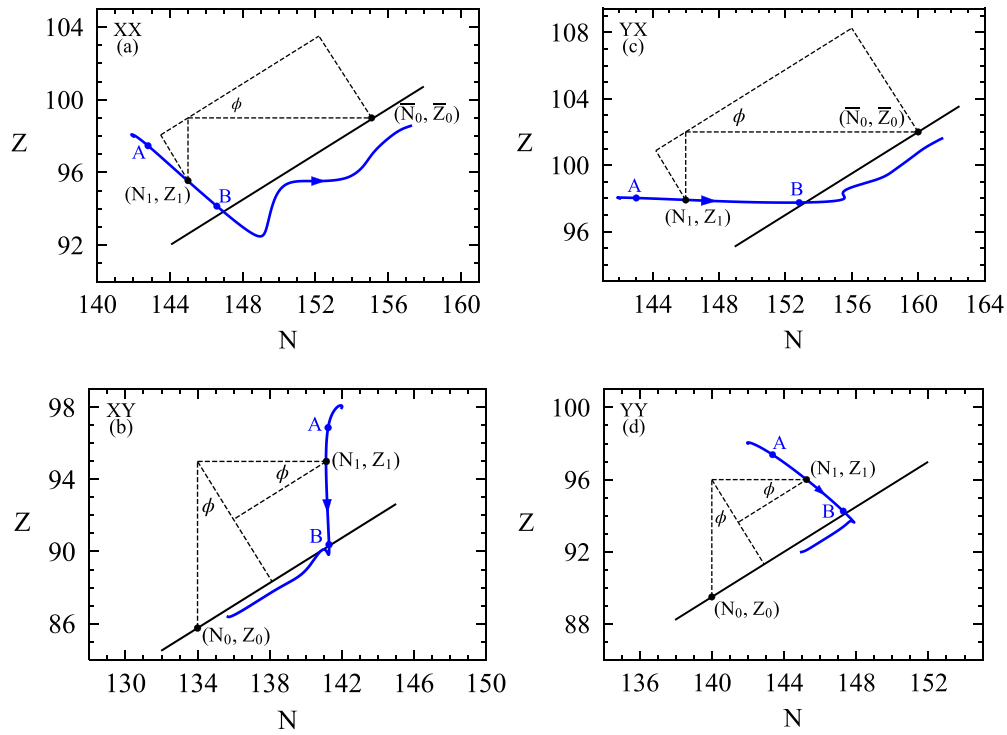

FIG. 3. Blue curves show the drift path of Cf-like fragments in the head-on collision of the ^{240}Cf + ^{246}Th system at $E_{\text{c.m.}} = 950$ MeV in tip-tip (XX), tip-side (XY), side-tip (YX), and side-side (YY) geometries. Labels A and B indicate intervals used in determining the average values of the reduced isovector curvature parameter α in Eqs. (12)–(14).

values of macroscopic variables. On the other hand, the time evolution of macroscopic variables becomes very important for the diffusion mechanism, as we discuss in Sec. IV. The blue curves in Fig. 1 show drift paths in head-on collisions of different geometries for Cf-like fragments. In these figures, thick black lines indicate equilibrium charge asymmetry with $(N-Z)/(N+Z)=0.22$. This line is referred to as the isoscalar path, which follows nearly parallel to the bottom of the stability line. The isoscalar path extends all the way toward the lead valley on one end, and toward the superheavy valley on the other end, making about a $\phi = 32^\circ$ angle with respect to the horizontal neutron axis. We observe that in all geometries,Cf-like fragments drift nearly along the isoscalar direction with charge asymmetry approximately equal to 0.22. Figure 1(a) shows the drift path for the tip-tip collision. As usually observed in quasifission reactions, Cf-like heavy fragments lose nucleons and the system drifts toward symmetry. In the side-tip collision, shown in Fig. 1(c), the nucleon drift mechanism is very different than the tip-tip geometry. Here, the heavy fragment gains neutrons and protons and the system drifts along the isoscalar path toward asymmetry. This kind of drift path is not very common, and it is referred to as the inverse quasifission reaction. Figure 1(d) shows the drift path for the side-side collision. The drift path in side-side collisions is different than other geometries. It appears that a small number of nucleons transfer, and the neutron and proton numbers of the final fragments are nearly the same as those of the initial fragments. This observation seems to indicate a particular result of shell effects in the side-side collision geometry. As a result, the dinuclear system wanders in the vicinity of a local equilibrium state of the potential energy surface in the N-Z plane without a noticeable drift in the symmetry or asymmetry directions. As seen in Fig. 1(b), in the tip-side collision, the nucleon drift mechanism is very different than those in other geometries. The dinuclear system drifts along the isoscalar path with the same charge asymmetry toward symmetry. However, Cf-like heavy fragments continue to lose neutrons and protons until they nearly reach thorium at the exit channel. In Ref. [52], this type of drift was named as the swap inverse quasifission reaction.

III. QUANTAL DIFFUSION DESCRIPTION

A. Langevin equation for nucleon transfer

The ordinary TDHF provides a deterministic description for collision dynamics. A single-particle density matrix is calculated with a given initial condition which is characterized by a single Slater determinant. On the other hand, due to correlations the actual initial state cannot be a single determinant but should be a superposition of Slater determinants. In the SMF approach, the correlated initial sate is represented by an ensemble of single-particle density matrices which are specified in terms of initial correlations [45,51]. Time evolution of the single-particle density matrix in each event in the ensemble is determined by the TDHF equations with the self-consistent Hamiltonian of that event. In each event of the SMF approach, fluctuations of the random elements of the initial density matrices are determined by Gaussian distributions the variances of which are specified with the requirement that the ensemble average of dispersions of one body observables in the initial state matches the quantal expressions in the mean-field approach.

When a dinuclear structure is maintained in the collision dynamics, as in the case of heavy-ion collisions at near barrier energies, we do not need to generate an ensemble of mean-field events. Instead, it is possible to develop a much easier transport description by employing the Langevin formalism for the relevant macroscopic variables. This is accomplished via a geometric projection of the SMF approach by utilizing the window dynamics. For the details of the quantal diffusion description and the window dynamics we refer to Refs. [56–64]. For the description of the nucleon diffusion mechanism, we consider neutron number and proton number of the projectilelike or targetlike fragments as the relevant macroscopic variables. In this paper, neutron $N_1^\lambda(t)$ and proton $Z_1^\lambda(t)$ numbers of the Cf-like fragments denote these variables. We can determine neutron and proton numbers of these fragments, for the event λ, by integrating the particle density on the left side or the right side of the dividing window. During contact, as a result of nucleon flux across the window, neutron and proton numbers of these fragments fluctuate from one event to another, and these numbers can be decomposed as $N_1^\lambda(t) = N_1(t) + \delta N_1^\lambda(t)$ and $Z_1^\lambda(t) = Z_1(t) + \delta Z_1^\lambda(t)$, where $N_1(t)$ and $Z_1(t)$ are the mean values taken over an ensemble of SMF events. For small amplitude fluctuations, these mean values are determined by the mean-field description of the TDHF theory. According to quantal diffusion approach, small amplitude fluctuations of the neutron $\delta N_1^\lambda(t)$ and proton $\delta Z_1^\lambda(t)$ numbers evolve as a coupled linear quantal Langevin equation [56–62]:

$$\frac{d}{dt}\begin{pmatrix}\delta Z_1^\lambda(t)\\ \delta N_1^\lambda(t)\end{pmatrix} = \begin{pmatrix}\frac{\partial v_p}{\partial Z_1}\left(Z_1^\lambda - Z_1\right) + \frac{\partial v_p}{\partial N_1}\left(N_1^\lambda - N_1\right)\\ \frac{\partial v_n}{\partial Z_1}\left(Z_1^\lambda - Z_1\right) + \frac{\partial v_n}{\partial N_1}\left(N_1^\lambda - N_1\right)\end{pmatrix} + \begin{pmatrix}\delta v_p^\lambda(t)\\ \delta v_n^\lambda(t)\end{pmatrix}. \quad (1)$$

Quantities $v_\alpha^\lambda(t) = v_\alpha(t) + \delta v_\alpha^\lambda(t)$ are the drift coefficients of neutrons and protons with the mean values and the fluctuating parts denoted by $v_\alpha(t)$ and $\delta v_\alpha^\lambda(t)$, respectively, with index α indicating neutron and proton labels. Drift coefficients $v_\alpha^\lambda(t)$ represent the rate of neutron and proton flux across the window for the event λ. The linear limit of Langevin description presented here provides a good approximation when the driving potential energy is nearly harmonic around the equilibrium values of the mass and charge asymmetry. The mean values of the drift coefficients are determined from the rate of change of neutron and proton numbers in Cf-like fragments, which are shown in Fig. 8 in the Appendix. The explicit quantal expressions of the stochastic parts of the drift coefficients $\delta v_\alpha^\lambda(t)$ can be found in Ref. [57].

B. Quantal diffusion coefficients

The stochastic parts of the drift coefficients $\delta v_p^\lambda(t)$ and $\delta v_n^\lambda(t)$ provide the source for generating fluctuations in

mass and charge asymmetry degrees of freedom. According to the SMF approach, stochastic parts of drift coefficients have Gaussian random distributions with zero mean values $\delta\overline{v}_p^{\lambda}(t) = 0$ and $\delta\overline{v}_n^{\lambda}(t) = 0$, and the autocorrelation functions of the stochastic drift coefficient integrated over the history determine diffusion coefficients $D_{\alpha\alpha}(t)$ for proton and neutron transfers:

$$\int_0^t dt' \overline{\delta v_\alpha^{\lambda}(t)\delta v_\alpha^{\lambda}(t')} = D_{\alpha\alpha}(t). \tag{2}$$

In general diffusion coefficients involve a complete set of particle-hole states. It is possible to eliminate the entire set of particle states by employing closure relations in the diabatic limit. This results in an important simplification, and as a result diffusion coefficients are determined entirely in terms of the occupied single-particle wave functions of TDHF evolution. Explicit expressions of the diffusion coefficients are provided in previous publications [56–62] and for the analysis of these coefficients please see Appendix B in Ref. [57]. The fact that diffusion coefficients are determined by the mean-field properties is consistent with the fluctuation dissipation theorem of nonequilibrium statistical mechanics and it greatly simplifies calculations of quantal diffusion coefficients. Diffusion coefficients include quantal effects due to shell structure, Pauli blocking, and the full effect of the collision geometry without any adjustable parameters. We observe that there is a close analogy between the quantal expression and the classical diffusion coefficient for a random walk problem [65–67]. The direct part is given as the sum of the nucleon currents across the window from the targetlike fragment to the projectilelike fragment and from the projectilelike fragment to the targetlike fragment, which is integrated over the memory. This is analogous to the random walk problem, in which the diffusion coefficient is given by the sum of the rate of the forward and backward steps. The second part in the quantal diffusion expression stands for the Pauli blocking effects in the nucleon transfer mechanism, which does not have a classical counterpart. As examples, Fig. 2 shows the neutron and proton diffusion coefficients in head-on collisions of the ^{250}Cf + ^{232}Th system at $E_{\text{c.m.}} = 950$ MeV for different collision geometries.

C. Potential energy of the dinuclear system

After colliding nuclei form a dinuclear system, the nucleon drift mechanism is determined via the potential energy surface in the (N, Z) plane. Potential energy of the dinuclear system $U(N_1, Z_1)$ primarily consists of the surface energy, electrostatic energy, symmetry energy, and centrifugal potential energy. TDHF theory includes different energy contributions microscopically. Furthermore, TDHF calculations show that the potential energy depends on the collision geometry. To compute the coupled Langevin equations, in addition to the diffusion coefficients, we need to evaluate derivatives of the mean drift coefficients with respect to neutron and proton numbers. The Einstein relations in the overdamped limit [56–62] provide a convenient approach to determine these derivatives. In the overdamped limit, drift coefficients are related to the potential energy surface in the (N, Z) plane as

$$v_n(t) = -\frac{D_{NN}(t)}{T^*}\frac{\partial}{\partial N_1}U(N_1, Z_1), \tag{3a}$$

$$v_z(t) = -\frac{D_{ZZ}(t)}{T^*}\frac{\partial}{\partial Z_1}U(N_1, Z_1), \tag{3b}$$

where T^* represents the effective temperature of the system. In heavy dinuclear systems, the centrifugal potential energy is not very important. Therefore, we ignore the centrifugal potential energy and analyze potential energy of dinuclear systems formed in head-on collisions with $\ell = 0$ relative angular momentum. In four geometries that we consider, the dinuclear system drifts along the isoscalar path toward a local equilibrium state. For collisions of actinide nuclei, the lighter local equilibrium state is located in the vicinity of the lead valley with neutron and proton numbers around $N_0 = 128$ and $Z_0 = 82$ and the heavier local equilibrium state is located in the vicinity of the superheavy valley with neutron and proton numbers around $\overline{N}_0 = N_T - N_0 = 166$ and $\overline{Z}_0 = Z_T - Z_0 = 106$. Here $N_T = 152 + 142$ is the total neutron number and $Z_T = 98 + 90$ is the total proton number of the dinuclear system, respectively. In Figs. 1 and 3 the solid black line indicates the isoscalar path with a constant charge asymmetry value $(N - Z)/(N + Z) = 0.22$. In the collisions of Cf + Th, drift in different collision geometries follows nearly this isoscalar path. The lead isotope with $Z = 82$ and $N = 128$ is located on this isoscalar path. We take this isotope as the local equilibrium reference state rather than $Z = 82$ and $N = 126$. This does not introduce an appreciable difference in the calculations of the reduced curvature parameter. As illustrated in Fig. 1, the dinuclear system formed in collision of ^{250}Cf + ^{232}Th drifts nearly along the isoscalar path, which is parallel to the equilibrium valley of stable nuclei. To extract information about potential energy in perpendicular direction to the stability valley, we need to choose the reaction of a suitable neighboring system. For this purpose, the head-on collision of the ^{240}Cf + ^{246}Th system provides a suitable system. Figure 3 shows the drift path of Cf-like fragments in the head-on collision of the ^{240}Cf + ^{246}Th reaction at tip-tip (XX), tip-side (XY), side-tip (YX), and side-side (YY) geometries at $E_{\text{c.m.}} = 950$ MeV. In the Appendix, Fig. 9 shows neutron and proton numbers of Cf fragments as a function of time in different geometries. In this system, the initial charge asymmetry of ^{240}Cf is $(N - Z)/(N + Z) = 0.18$ and that of ^{246}Th is $(N - Z)/(N + Z) = 0.27$. Initially, the system rapidly drifts towards the equilibrium valley, until it reaches equilibrium charge asymmetry value 0.22. The perpendicular component of this drift line is referred to as the isovector path. Then, the system continues to drift along the isoscalar path toward symmetry or asymmetry with the same charge asymmetry and the same slope angle as the isoscalar path in the ^{250}Cf + ^{232}Th system. The system separates before reaching local equilibrium. Combining the drift information of these two very similar systems, we can provide an approximate description of the potential energy surface of the dinuclear system relative to the equilibrium value in terms of

two parabolic forms [68]:

$$U(N_1, Z_1) = \tfrac{1}{2} a R_S^2(N_1, Z_1) + \tfrac{1}{2} b R_V^2(N_1, Z_1). \quad (4)$$

Here, $R_S(N_1, Z_1)$ and $R_V(N_1, Z_1)$ represent perpendicular distances of a fragment with neutron and proton numbers (N_1, Z_1) from the isoscalar path and from the local equilibrium state along the isoscalar path, respectively. Because of the sharp increase of asymmetry energy, we expect the isovector curvature parameter a to be much larger than the isoscalar curvature parameter b. When drift occurs toward symmetry like in Fig. 3(d), we can express the isoscalar distance from the local equilibrium state (N_0, Z_0) as $R_V = (N_1 - N_0)\cos\phi + (Z_1 - Z_0)\sin\phi$, and the isovector distance from the isoscalar path as $R_S = (Z_1 - Z_0)\cos\phi - (N_1 - N_0)\sin\phi$. When drift occurs toward asymmetry like in Fig. 3(c), we can express isoscalar distance from the local equilibrium state $(\overline{N}_0, \overline{Z}_0)$ as $\overline{R}_V = (\overline{N}_0 - N_1)\cos\phi + (\overline{Z}_0 - Z_1)\sin\phi$, and the isovector distance as $\overline{R}_S = (\overline{N}_0 - N_1)\sin\phi - (\overline{Z}_0 - Z_1)\cos\phi$. The angle ϕ is the angle between the isoscalar path and the N axis, which is about $\phi = 32^\circ$. It is possible to derive similar expressions for other geometries. All have the same isoscalar path which makes the same angle $\phi = 32^\circ$ with the N axis. Because of analytical relations of the potential energy in the Einstein relations, we can immediately calculate derivatives of drift coefficients to find

$$\frac{\partial v_n}{\partial N_1} = -D_{NN}(\alpha \sin^2\phi + \beta \cos^2\phi), \quad (5)$$

$$\frac{\partial v_z}{\partial Z_1} = -D_{ZZ}(\alpha \cos^2\phi + \beta \sin^2\phi), \quad (6)$$

$$\frac{\partial v_n}{\partial Z_1} = -D_{NN}(\beta - \alpha)\sin\phi\cos\phi, \quad (7)$$

$$\frac{\partial v_z}{\partial N_1} = -D_{ZZ}(\beta - \alpha)\sin\phi\cos\phi. \quad (8)$$

These expressions are valid for different collision geometries with different values of reduced isoscalar, $\beta = b/T^*$, and isovector, $\alpha = a/T^*$, curvature parameters. By inverting Eqs. (3a) and (3b), it is possible to express the reduced curvature parameters in terms of drift and diffusion coefficients. Due to microscopic shell structure, transport coefficients depend on time, and as a result the reduced curvature parameters are time dependent as well. In simple parabolic parametrization of the potential energy surface, we ignore the time dependence and use constant curvature parameters. Constant curvature parameters are determined by averaging over suitable time intervals while colliding nuclei have sufficiently large overlap. When drift occurs toward symmetry, the averaged value of the isoscalar reduced curvature parameter over a time interval t_1 and t_2 is determined as

$$\beta(12) = -\frac{1}{R_V(12)} \int_{t_1}^{t_2} \left(\frac{v_n(t)\cos\phi}{D_{NN}(t)} + \frac{v_p(t)\sin\phi}{D_{ZZ}(t)} \right) dt, \quad (9)$$

where the integrated isoscalar distance is given by

$$R_V(12) = \int_{t_1}^{t_2} \{[N_1(t) - N_0]\cos\phi + [Z_1(t) - Z_0]\sin\phi\} dt. \quad (10)$$

We can use these expressions in calculating averaged values of isoscalar reduced curvature parameters in different geometries. In the tip-tip collision of the ^{250}Cf + ^{232}Th system, we take the averaging interval, as shown in Fig. 8(a) in the Appendix, as $t_1 \to t_A = 150$ fm/c and $t_2 \to t_B = 550$ fm/c, and we find the reduced isoscalar curvature parameter in tip-tip geometry to be $\beta(\mathrm{TT}) = 0.005$. In tip-side geometry using the interval as $t_1 \to t_A = 200$ fm/c and $t_2 \to t_B = 500$ fm/c, as shown in Fig. 8(b) of the Appendix, we find the reduced isoscalar curvature parameter in tip-side geometry to be $\beta(\mathrm{TS}) = 0.009$. When drift is toward asymmetry, we can determine the averaged value of the isoscalar reduced curvature parameter over a time interval t_1 and t_2 using the negative of Eq. (9) and, by taking the integrated isoscalar distance as $R_V(12) \to \overline{R}_V(12)$,

$$\overline{R}_V(12) = \int_{t_1}^{t_2} \left\{[\overline{N}_0 - N_1(t)]\cos\phi + [\overline{Z}_0 - Z_1(t)]\sin\phi\right\} dt. \quad (11)$$

In side-tip geometry, using the interval $t_A = 200$ fm/c and $t_B = 500$ fm/c, as shown in Fig. 8(c) in the Appendix, we find the reduced isoscalar curvature parameter to be $\beta(\mathrm{ST}) = 0.009$. For the side-side geometry, we estimate the isoscalar curvature parameters in the interval $t_A \to t_B$ with $t_A = 200$ fm/c and $t_B = 300$ fm/c, as shown in Fig. 8(d) in the Appendix, to be $\beta(\mathrm{SS}) = 0.004$. In the interval $t_B \to t_C$ with $t_B = 300$ fm/c and $t_C = 800$ fm/c, we estimate the isoscalar curvature parameter to have the same magnitude, $\beta(\mathrm{SS}) = 0.004$.

When drift occurs toward symmetry, we estimate the isovector reduced curvature parameters in different collision geometries from the drift paths of ^{240}Cf + ^{246}Th by averaging over time interval t_1 and t_2 as

$$\alpha(12) = \frac{1}{R_S(12)} \int_{t_1}^{t_2} \left(\frac{v_n(t)\sin\phi}{D_{NN}(t)} - \frac{v_p(t)\cos\phi}{D_{ZZ}(t)} \right) dt, \quad (12)$$

where the integrated isovector distance is given by

$$R_S(12) = \int_{t_1}^{t_2} \{[Z_1(t) - Z_0]\cos\phi - [N_1(t) - N_0]\sin\phi\} dt. \quad (13)$$

In side-side geometry, we estimate the isovector curvature parameter by calculating the average value in the interval $t_A \to t_B$ with $t_A = 220$ fm/c and $t_B = 310$ fm/c, as shown by Fig. 9(d) in the Appendix. We find the reduced isoscalar curvature parameter to be $\alpha(\mathrm{SS}) = 0.11$. In tip-side geometry, we estimate the isovector curvature parameter by calculating the average value in the interval $t_A \to t_B$ with $t_A = 170$ fm/c and $t_B = 280$ fm/c, as shown by Fig. 9(b) in the Appendix. We find the reduced isoscalar curvature parameter to be $\alpha(\mathrm{TS}) = 0.15$. When drift occurs toward asymmetry, we estimate the isovector reduced curvature parameters in different collision geometries from the drift paths of ^{240}Cf + ^{246}Th using Eq. (12) in which the integrated isovector distance is

replaced by $R_S(12) \to \overline{R}_S(12)$:

$$\overline{R}_S(12) = \int_{t_1}^{t_2} \left\{[\overline{Z}_0 - Z_1(t)]\cos\phi - [\overline{N}_0 - N_1(t)]\sin\phi\right\} dt. \tag{14}$$

In side-tip geometry, we estimate the isovector curvature parameter by calculating the average value in the interval $t_A \to t_B$ with $t_A = 150$ fm/c and $t_B = 260$ fm/c, as shown by Fig. 9(c) in the Appendix. We find the reduced isoscalar curvature parameter to be $\alpha(\mathrm{ST}) = 0.12$. In tip-tip geometry, we estimate the isovector curvature parameter by calculating the average value in the interval $t_A \to t_B$ with $t_A = 150$ fm/c and $t_B = 220$ fm/c, as shown by Fig. 9(a) in the Appendix. We find the reduced isoscalar curvature parameter to be $\alpha(\mathrm{TT}) = 0.16$.

IV. PRIMARY AND SECONDARY CROSS SECTIONS OF REACTION PRODUCTS

A. Probability distributions of primary fragments

The joint probability distribution function $P_\ell(N, Z)$ for producing binary fragments with N neutrons and Z protons is determined by generating a large number of solutions of the Langevin Eq. (1). It is well known that the Langevin equation is equivalent to the Fokker-Planck equation for the distribution function of the macroscopic variables [65]. In the special case, when drift coefficients are linear functions of macroscopic variables, as we have in Eq. (1), the proton and neutron distribution function for the initial orbital angular momentum ℓ is given as a correlated Gaussian function described by the mean values and neutron, proton, and mixed dispersions as

$$P_\ell(N, Z) = \frac{1}{2\pi\sigma_{NN}(\ell)\sigma_{ZZ}(\ell)\sqrt{1-\rho_\ell^2}} \exp(-C_\ell). \tag{15}$$

Here, the exponent C_l for each initial angular momentum is given by

$$C_\ell = \frac{1}{2(1-\rho_\ell^2)}\left[\left(\frac{Z-Z_\ell}{\sigma_{ZZ}(\ell)}\right)^2 - 2\rho_\ell\left(\frac{Z-Z_\ell}{\sigma_{ZZ}(\ell)}\right)\left(\frac{N-N_\ell}{\sigma_{NN}(\ell)}\right) + \left(\frac{N-N_\ell}{\sigma_{NN}(\ell)}\right)^2\right], \tag{16}$$

with the correlation coefficient defined as $\rho_\ell = \sigma_{NZ}^2(\ell)/[\sigma_{ZZ}(\ell)\sigma_{NN}(\ell)]$. Quantities $N_\ell = \overline{N}_\ell^\lambda$ and $Z_\ell = \overline{Z}_\ell^\lambda$ denote the mean neutron and proton numbers of the targetlike or projectilelike fragments. These mean values are determined from the TDHF calculations. It is possible to deduce coupled differential equations for variances $\sigma_{NN}^2(\ell) = \overline{\delta N^\lambda \delta N^\lambda}$ and $\sigma_{ZZ}^2(\ell) = \overline{\delta Z^\lambda \delta Z^\lambda}$ and covariances $\sigma_{NZ}^2(\ell) = \overline{\delta N^\lambda \delta Z^\lambda}$ by multiplying Langevin Eq. (1) with δN^λ and δZ^λ and carrying out the average over the ensemble generated from the solution of the Langevin equation. These coupled equations were presented in Refs. [56–62]. For completeness, we provide these differential equations here [69]:

$$\frac{\partial}{\partial t}\sigma_{NN}^2 = 2\frac{\partial \nu_n}{\partial N_1}\sigma_{NN}^2 + 2\frac{\partial \nu_n}{\partial Z_1}\sigma_{NZ}^2 + 2D_{NN}, \tag{17}$$

$$\frac{\partial}{\partial t}\sigma_{ZZ}^2 = 2\frac{\partial \nu_p}{\partial Z_1}\sigma_{ZZ}^2 + 2\frac{\partial \nu_p}{\partial N_1}\sigma_{NZ}^2 + 2D_{ZZ}, \tag{18}$$

and

$$\frac{\partial}{\partial t}\sigma_{NZ}^2 = \frac{\partial \nu_p}{\partial N_1}\sigma_{NN}^2 + \frac{\partial \nu_n}{\partial Z_1}\sigma_{ZZ}^2 + \sigma_{NZ}^2\left(\frac{\partial \nu_p}{\partial Z_1} + \frac{\partial \nu_n}{\partial N_1}\right). \tag{19}$$

Here, D_{NN} and D_{ZZ} indicate the diffusion coefficients for proton and neutron transfer. Variances and covariances are determined from the solutions of these coupled differential equations with initial conditions $\sigma_{NN}^2(t=0) = 0$, $\sigma_{ZZ}^2(t=0) = 0$, and $\sigma_{NZ}^2(t=0) = 0$, for each orbital angular momentum. As an example, Fig. 4 shows neutron, proton, and mixed variances, as a function of time, in the head-on collision of Cf + Th at $E_{\mathrm{c.m.}} = 950$ MeV for the tip-tip tip-side, side-tip, and side-side collision geometries.

B. Cross sections of primary reaction products

We calculate the cross sections for production of primary isotopes using the standard expression:

$$\sigma^{\mathrm{pri}}(N, Z) = \frac{\pi\hbar^2}{2\mu E_{\mathrm{c.m.}}} \sum_{\ell_{\min}}^{\ell_{\max}} (2\ell+1) P_\ell^{\mathrm{pri}}(N, Z), \tag{20}$$

where

$$P_\ell^{\mathrm{pri}}(N, Z) = \tfrac{1}{2}\left[P_\ell^{\mathrm{pro}}(N, Z) + P_\ell^{\mathrm{tar}}(N, Z)\right]. \tag{21}$$

In this expression, $P_\ell^{\mathrm{pro}}(N, Z)$ and $P_\ell^{\mathrm{tar}}(N, Z)$ denote the normalized probability of producing projectilelike and targetlike fragments. These probabilities are given by Eq. (15) using mean values of projectilelike and targetlike fragments, respectively. The factor of $1/2$ is introduced to make the total primary fragment distribution normalized to unity. In summation over ℓ, the range of initial orbital angular momenta depends on the detector geometry in the laboratory frame. There are no nucleon transfer data available for the ^{250}Cf + ^{232}Th system. In calculations, we carry out summation over the range from $\ell_{\min} = 0\hbar$ to $\ell_{\max} = 480\hbar$. The upper limit corresponds to quasi-elastic-scattering events with a few nucleon transfer channels. We calculate total double cross sections for four different tip-tip, tip-side, side-tip, and side-side collision geometries. Figure 5 shows the double cross sections in the N-Z plane for the production of primary fragments in tip-tip (a), tip-side (b), side-tip (c), and side-side (d) geometries. The points shown by crosses indicate colliding nuclei ^{250}Cf and ^{232}Th. Equal values of primary cross sections form elliptic curves. Large values of mixed dispersions indicate strong correlations in neutron-proton transfers. The strong correlations are induced mainly by the symmetry energy. As a result, the major axes of equal cross-section elliptic curves are aligned along with the valley of stability. Gross properties of primary cross sections are similar in different collision geometries. Due to the drift towards asymmetry direction, magnitude of the cross sections along the isoscalar

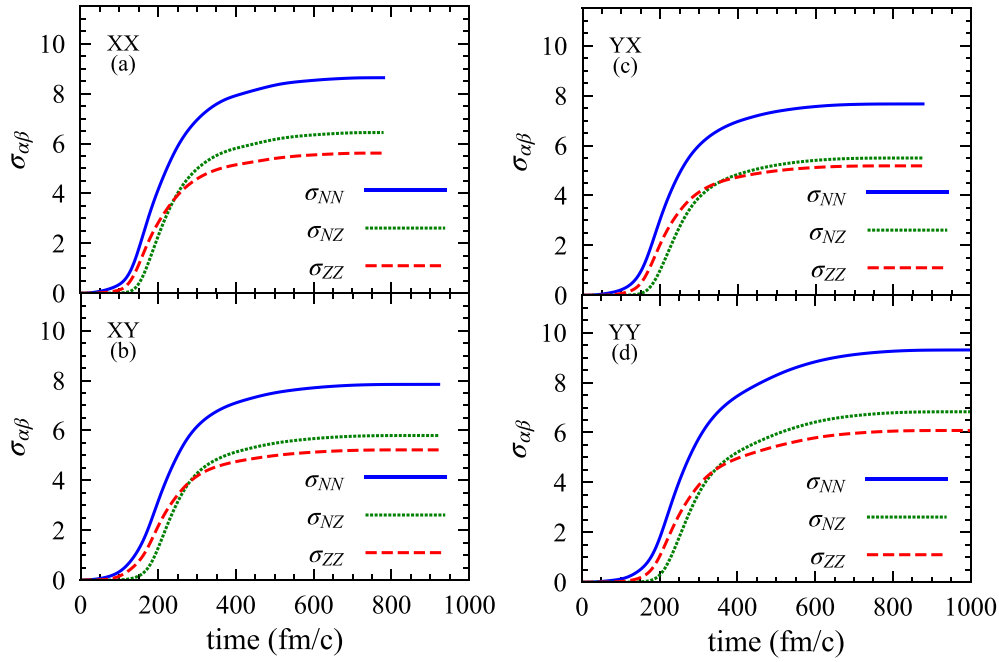

FIG. 4. Neutron, proton, and mixed variances as a function of time in the ^{250}Cf + ^{232}Th system at $E_{\text{c.m.}} = 950$ MeV in tip-tip (XX), tip-side (XY), side-tip (YX), and side-side (YY) geometries.

direction extends further towards the superheavy island in side-tip collision geometry as compared to the other collision geometries. As an example, magnitude of the primary cross section for production of elements ($Z = 118$, $N = 185$) is about 0.01 mb, which is larger than those in other collision geometries.

C. Cross sections of secondary reaction products

Primary fragments are excited and cooled down by light particle emission, mostly neutrons, protons, and alpha particles, or they may decay via binary fission. We analyze the deexcitation mechanisms of the primary fragments using the statistical code GEMINI++ [70]. We estimate the total excitation energy of the primary fragments according to $E^*_\ell(Z,N) = E_{\text{c.m.}} - \text{TKE}_\ell - Q_{\text{gg}}(Z,N)$. In this expression TKE_ℓ is the mean value of total asymptotic kinetic energy in collision with initial orbital angular momentum ℓ, and $Q_{\text{gg}}(Z,N)$ denotes the ground state Q value of the primary fragments relative to the initial value. For collisions with an initial orbital angular momentum, in the exit channel total spin and total excitation energy should have distributions around their mean values. In the present analysis, we ignore the fluctuations in excitation energy and spin of primary fragments. We share the mean value of the total excitation energy and the total angular momentum transfer in proportion to mass ratio of the primary fragments. The excited parent nucleus decays by a series of particle emissions and by secondary fission until the decay of the parent nucleus is energetically forbidden. Starting from an excited parent nucleus with neutron and proton numbers (Z,N), excitation energy $E^*(Z,N)$, and spin J, statistical code GEMINI++ determines the probability $W(N,Z \to N',Z')$ of reaching final nucleus (Z',N'). The probability distribution of secondary fragments is specified as

$$P^{\text{sec}}_\ell(N',Z') = \sum_{N \geqslant N'} \sum_{Z \geqslant Z'} P^{\text{pri}}_\ell(N,Z) W(N,Z \to N',Z'). \quad (22)$$

Here, summation (Z,N) covers the pairs of projectilelike fragments and targetlike fragments of the dinuclear system according to their probability distributions:

$$\sigma^{\text{sec}}_\ell(N',Z') = \frac{\pi\hbar^2}{2\mu E_{\text{c.m.}}} \sum_{\ell_{\text{min}}}^{\ell_{\text{max}}} (2\ell+1) P^{\text{sec}}_\ell(N',Z'). \quad (23)$$

Figure 6 shows the double cross sections of secondary fragments in the N-Z plane for different collision geometries. Again, the gross properties of the secondary cross sections are very similar for different collision geometries. Below $N = 100$ and $Z = 60$, decay products consist of secondary fission of excited heavy fragments. Above this region the cross sections are populated by light particle emission including neutron, proton, and alpha particles. Calculations predict production of a broad range of neutron rich isotopes for nuclei with proton numbers in the range of $Z = 70$–90, with cross sections on the order of several hundred microbarns. Figure 7 shows an enlarged view of the secondary cross sections for heavy neutron rich nuclei for the range of proton numbers $Z = 80$–90 and the range of neutron numbers $N = 130$–160. Furthermore, our calculations indicate a number of neutron rich heavy isotopes with sizable cross sections including ^{246}Cm with a cross section of 159 nb for the side-side collision, ^{248}Cm with a cross section of 80 nb for the tip-side collision, and ^{253}Cm with a cross section of 252 nb for the side-tip collision. In reality, all collision orientations contribute to the cross sections and one should weigh each one with an appropriate geometric factor. As a result, the values provided

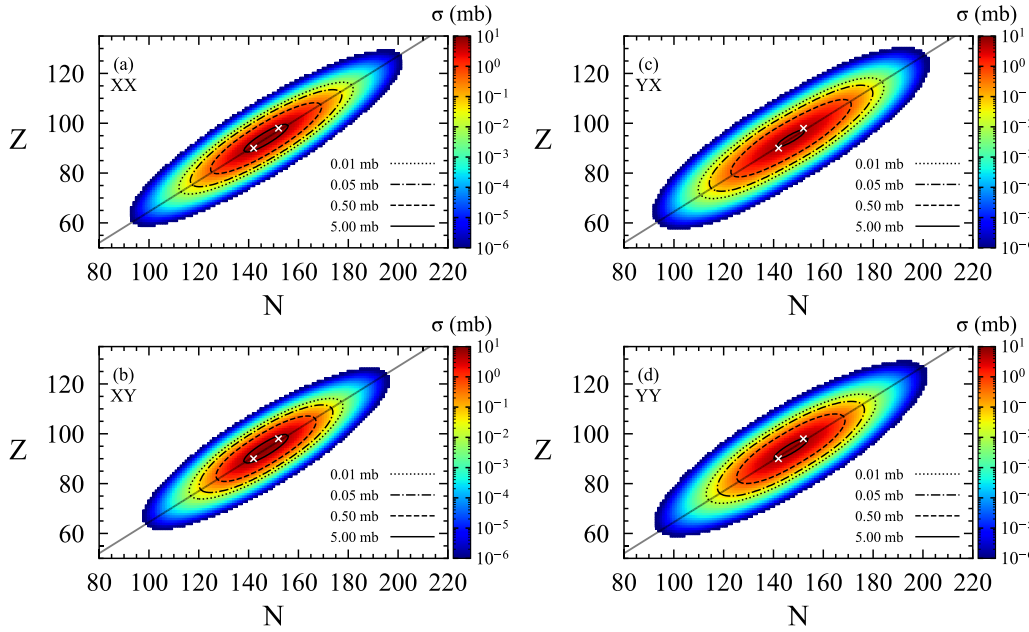

FIG. 5. Primary production cross sections in the N-Z plane for the $^{250}\mathrm{Cf} + ^{232}\mathrm{Th}$ system at $E_{\mathrm{c.m.}} = 950$ MeV in tip-tip (XX), tip-side (XY), side-tip (YX), and side-side (YY) geometries.

here should be seen as order of magnitude as well as upper limits.

V. CONCLUSIONS

We have presented an investigation of the multinucleon transfer mechanism for the collisions of the $^{250}\mathrm{Cf} + ^{232}\mathrm{Th}$ system at $E_{\mathrm{c.m.}} = 950$ MeV employing the quantal transport description based on the SMF approach. The standard mean-field description of TDHF determines average evolution of the most probable path of heavy-ion collision dynamics at low energies. The SMF provides an extension to the standard TDHF description by including mean-field fluctuations in a manner consistent with the fluctuation-dissipation theorem of nonequilibrium statistical mechanics. When a dinuclear complex is maintained in collisions, we can extract Langevin equations for macroscopic variables, such as the mass and charge asymmetry of colliding ions. In this paper, we take

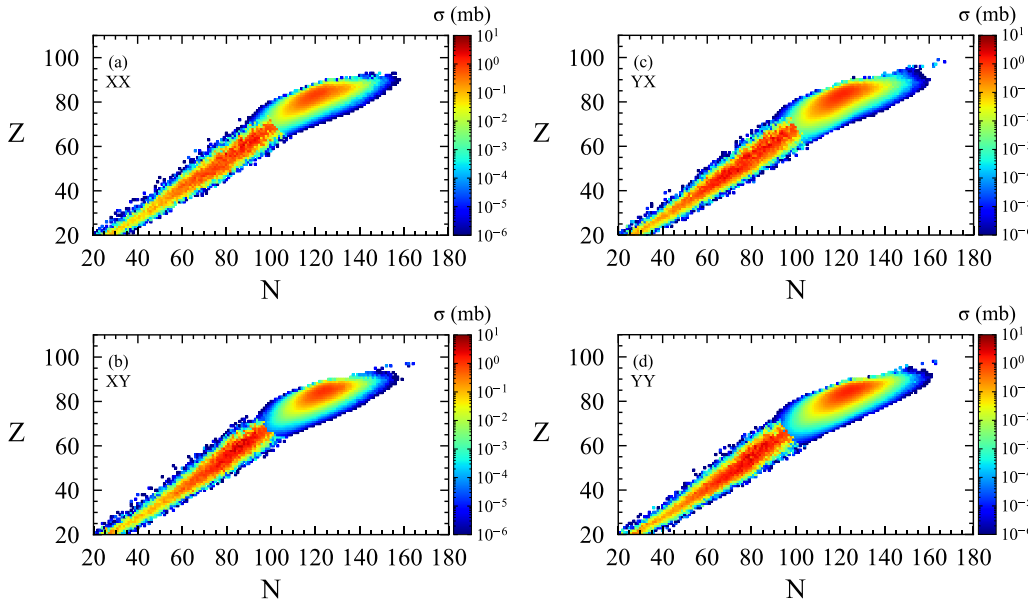

FIG. 6. Secondary production cross sections in the N-Z plane for the $^{250}\mathrm{Cf} + ^{232}\mathrm{Th}$ system at $E_{\mathrm{c.m.}} = 950$ MeV in tip-tip (XX), tip-side (XY), side-tip (YX), and side-side (YY) geometries.

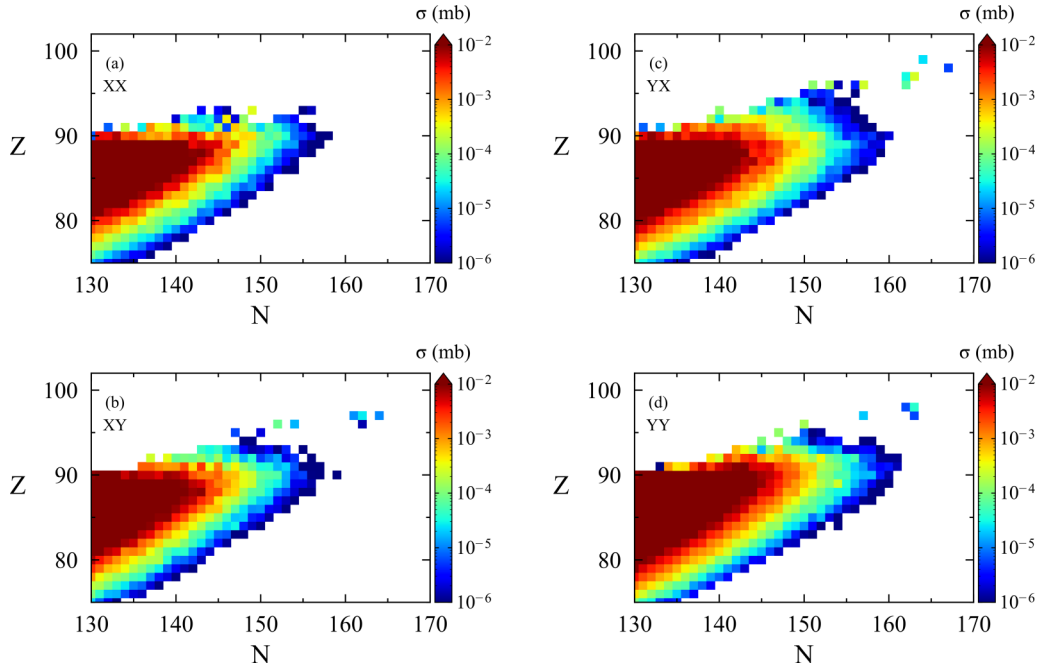

FIG. 7. Enlarged view of secondary production cross sections in the N-Z plane for the ^{250}Cf + ^{232}Th system at $E_{\text{c.m.}} = 950$ MeV in tip-tip (XX), tip-side (XY), side-tip (YX), and side-side (YY) geometries.

neutron and proton numbers of one of the collision partners in the dinuclear complex as the relevant macroscopic variables. Using the equivalence of Langevin description and Fokker-Planck descriptions, it is possible to provide nearly an analytical description in terms of correlated Gaussian shape probability distribution of the primary fragments produced in collisions. The correlated Gaussian distribution for each orbital angular momentum is determined by the asymptotic

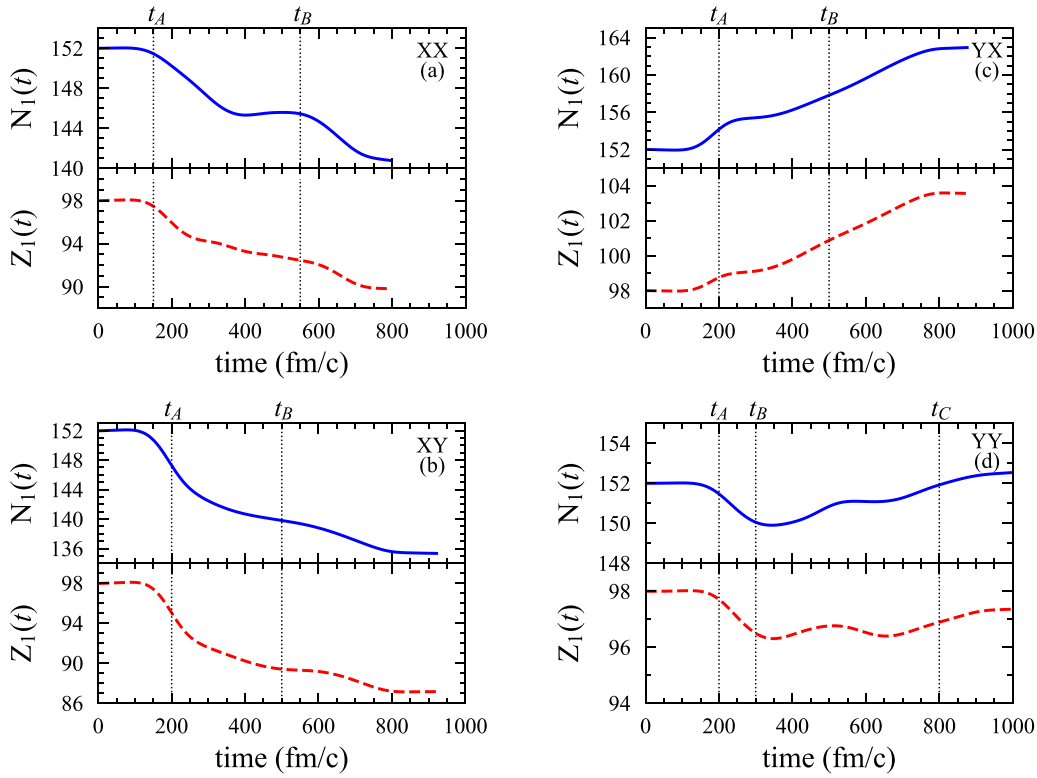

FIG. 8. Mean values of neutron and proton numbers of Cf-like fragments in the head-on collision of the ^{250}Cf + ^{232}Th system at $E_{\text{c.m.}} = 950$ MeV in tip-tip (XX), tip-side (XY), side-tip (YX), and side-side (YY) geometries.

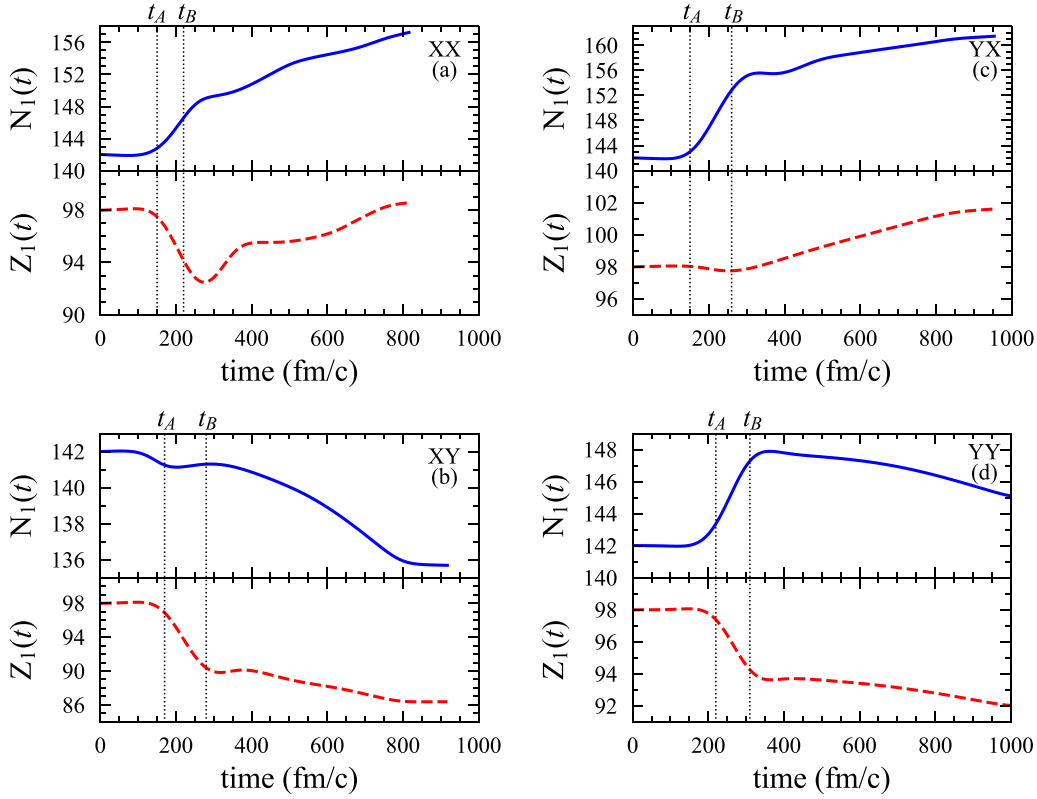

FIG. 9. Mean values of neutron and proton numbers of Cf-like fragments in the head-on collision of the ^{240}Cf + ^{246}Th system at $E_{\text{c.m.}} = 950$ MeV in tip-tip (XX), tip-side (XY), side-tip (YX), and side-side (YY) geometries.

values of the mean neutron and proton numbers of the primary fragments, and the neutron, proton, and mixed dispersions. We determine these dispersions employing the quantal transport approach. Diffusion coefficients, which provide the source for developing fluctuations, are evaluated in terms of the occupied single-particle wave functions of the TDHF theory. Transport coefficients include quantal effects due to shell structure and Pauli blocking, and do not involve any adjustable parameters

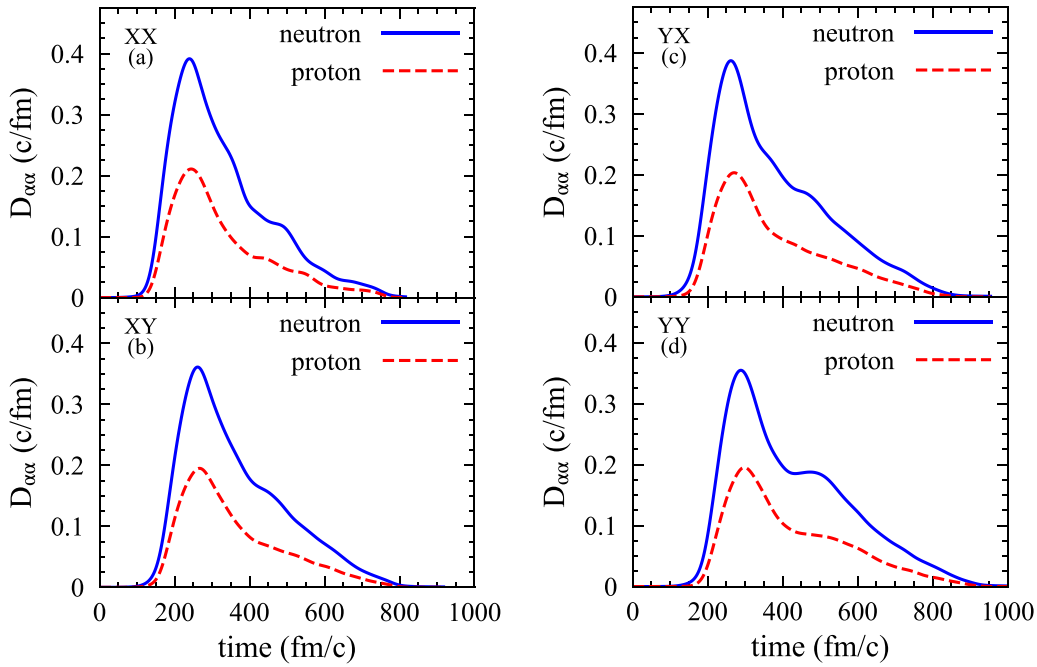

FIG. 10. Diffusion coefficients in the head-on collision of the ^{240}Cf + ^{246}Th system at $E_{\text{c.m.}} = 950$ MeV in tip-tip (XX), tip-side (XY), side-tip (YX), and side-side (YY) geometries.

other than the standard parameters of the effective Skyrme force used in the TDHF calculations. Highly excited primary fragments decay by particle emission and secondary fission. Employing the statistical code GEMINI++, we can follow the deexcitation process of primary fragments, and calculate the production cross sections for the secondary fragments. Since there are no data available, we are not able to test our prediction for the multinucleon transfer mechanism for the ^{250}Cf + ^{232}Th reaction.

ACKNOWLEDGMENTS

S.A. gratefully acknowledges Middle East Technical University for warm hospitality extended to him during his visits. S.A. also gratefully acknowledges F. Ayik for continuous support and encouragement. This work is supported in part by U.S. Department of Energy Grants No. DE-SC0015513 and No. DE-SC0013847. This work is supported in part by TUBITAK Grant No. 122F150. The numerical calculations reported in this paper were partially performed at TUBITAK ULAKBIM, High Performance and Grid Computing Center (TRUBA resources).

APPENDIX

We can estimate the averaged values of reduced isoscalar and isovector curvature parameters with the help of Einstein relations, Eqs. (3a) and (3b), in the overdamped limit. We evaluate the average values of the reduced curvature parameters for different geometries by carrying out the time integrals in Eqs. (9) and (12) over suitable time intervals. These time intervals are indicated in Figs. 8–10 for ^{250}Cf + ^{232}Th and ^{240}Cf + ^{246}Th reactions.

[1] A. Chatillon, Ch. Theisen, P. T. Greenlees, G. Auger, J. E. Bastin, E. Bouchez, B. Bouriquet, J. M. Casandjian, R. Cee, E. Clément, R. Dayras, G. de France, R. de Toureil, S. Eeckhaudt, A. Göergen, T. Grahn, S. Grévy, K. Hauschild, R.-D. Herzberg, P. J. C. Ikin *et al.*, Spectroscopy and single-particle structure of the odd-Z heavy elements ^{255}Lr, ^{251}Md and ^{247}Es, Eur. Phys. J. A **30**, 397 (2006).

[2] R.-D. Herzberg, P. T. Greenlees, P. A. Butler, G. D. Jones, M. Venhart, I. G. Darby, S. Eeckhaudt, K. Eskola, T. Grahn, C. Gray-Jones, F. P. Heßberger, P. Jones, R. Julin, S. Juutinen, S. Ketelhut, W. Korten, M. Leino, A.-P. Leppanen, S. Moon, M. Nyman *et al.*, Nuclear isomers in superheavy elements as stepping stones towards the island of stability, Nature (London) **442**, 896 (2006).

[3] E. M. Kozulin, E. Vardaci, G. N. Knyazheva, A. A. Bogachev, S. N. Dmitriev, I. M. Itkis, M. G. Itkis, A. G. Knyazev, T. A. Loktev, K. V. Novikov, E. A. Razinkov, O. V. Rudakov, S. V. Smirnov, W. Trzaska, and V. I. Zagrebaev, Mass distributions of the system ^{136}Xe + ^{208}Pb at laboratory energies around the Coulomb barrier: A candidate reaction for the production of neutron–rich nuclei at $N = 126$, Phys. Rev. C **86**, 044611 (2012).

[4] J. V. Kratz, M. Schädel, and H. W. Gäggeler, Reexamining the heavy-ion reactions ^{238}U + ^{238}U and ^{238}U + ^{248}Cm and actinide production close to the barrier, Phys. Rev. C **88**, 054615 (2013).

[5] Y. X. Watanabe, Y. H. Kim, S. C. Jeong, Y. Hirayama, N. Imai, H. Ishiyama, H. S. Jung, H. Miyatake, S. Choi, J. S. Song, E. Clement, G. de France, A. Navin, M. Rejmund, C. Schmitt, G. Pollarolo, L. Corradi, E. Fioretto, D. Montanari, M. Niikura *et al.*, Pathway for the Production of Neutron–Rich Isotopes Around the $N = 126$ Shell Closure, Phys. Rev. Lett. **115**, 172503 (2015).

[6] V. V. Desai, W. Loveland, K. McCaleb, R. Yanez, G. Lane, S. S. Hota, M. W. Reed, H. Watanabe, S. Zhu, K. Auranen, A. D. Ayangeakaa, M. P. Carpenter, J. P. Greene, F. G. Kondev, D. Seweryniak, R. V. F. Janssens, and P. A. Copp, The ^{136}Xe + ^{198}Pt reaction: A test of models of multi-nucleon transfer reactions, Phys. Rev. C **99**, 044604 (2019).

[7] G. G. Adamian, N. V. Antonenko, V. V. Sargsyan, and W. Scheid, Possibility of production of neutron-rich Zn and Ge isotopes in multinucleon transfer reactions at low energies, Phys. Rev. C **81**, 024604 (2010).

[8] G. G. Adamian, N. V. Antonenko, and D. Lacroix, Production of neutron-rich Ca, Sn, and Xe isotopes in transfer-type reactions with radioactive beams, Phys. Rev. C **82**, 064611 (2010).

[9] X. Jiang and N. Wang, Probing the production mechanism of neutron-rich nuclei in multinucleon transfer reactions, Phys. Rev. C **101**, 014604 (2020).

[10] G. G. Adamian, N. V. Antonenko, A. Diaz-Torres, and S. Heinz, How to extend the chart of nuclides?, Eur. Phys. J. A **56**, 47 (2020).

[11] S. A. Kalandarov, G. G. Adamian, N. V. Antonenko, H. M. Devaraja, and S. Heinz, Production of neutron deficient isotopes in the multinucleon transfer reaction ^{48}Ca ($E_{\rm lab}$ = 5.63MeV/nucleon) + ^{248}Cm, Phys. Rev. C **102**, 024612 (2020).

[12] C. Li, J. Tian, and F. Zhang, Production mechanism of the neutron-rich nuclei in multinucleon transfer reactions: A reaction time scale analysis in energy dissipation process, Phys. Lett. B **809**, 135697 (2020).

[13] G. G. Adamian, N. V. Antonenko, H. Lenske, L. A. Malov, and S. Zhou, Self-consistent methods for structure and production of heavy and superheavy nuclei, Eur. Phys. J. A **57**, 89 (2021).

[14] M. G. Itkis, G. N. Knyazheva, I. M. Itkis, and E. M. Kozulin, Experimental investigation of cross sections for the production of heavy and superheavy nuclei, Eur. Phys. J. A **58**, 178 (2022).

[15] S. Heinz and H. M. Devaraja, Nucleosynthesis in multinucleon transfer reactions, Eur. Phys. J. A **58**, 114 (2022).

[16] Z. Wu, L. Guo, Z. Liu, and G. Peng, Production of proton-rich nuclei in the vicinity of ^{100}Sn via multinucleon transfer reactions, Phys. Lett. B **825**, 136886 (2022).

[17] S. Hofmann and G. Münzenberg, The discovery of the heaviest elements, Rev. Mod. Phys. **72**, 733 (2000).

[18] Yu. Ts. Oganessian, V. K. Utyonkov, Yu. V. Lobanov, F. Sh. Abdullin, A. N. Polyakov, R. N. Sagaidak, I. V. Shirokovsky, Yu. S. Tsyganov, A. A. Voinov, G. G. Gulbekian, S. L. Bogomolov, B. N. Gikal, A. N. Mezentsev, S. Iliev, V. G. Subbotin, A. M. Sukhov, K. Subotic, V. I. Zagrebaev, G. K. Vostokin, M. G. Itkis *et al.*, Synthesis of the isotopes of elements 118 and 116 in the ^{249}Cf and ^{245}Cm + ^{48}Ca fusion reactions, Phys. Rev. C **74**, 044602 (2006).

[19] V. I. Zagrebaev, Yu. Ts. Oganessian, M. G. Itkis, and W. Greiner, Superheavy nuclei and quasi-atoms produced in collisions of transuranium ions, Phys. Rev. C **73**, 031602(R) (2006).

[20] Valery Zagrebaev and Walter Greiner, New way for the production of heavy neutron-rich nuclei, J. Phys. G: Nucl. Part. Phys. **35**, 125103 (2008).

[21] Valery Zagrebaev and Walter Greiner, Production of New Heavy Isotopes in Low–Energy Multinucleon Transfer Reactions, Phys. Rev. Lett. **101**, 122701 (2008).

[22] V. I. Zagrebaev and W. Greiner, Production of heavy and superheavy neutron-rich nuclei in transfer reactions, Phys. Rev. C **83**, 044618 (2011).

[23] A. V. Karpov and V. V. Saiko, Modeling near-barrier collisions of heavy ions based on a Langevin-type approach, Phys. Rev. C **96**, 024618 (2017).

[24] V. V. Saiko and A. V. Karpov, Analysis of multinucleon transfer reactions with spherical and statically deformed nuclei using a Langevin-type approach, Phys. Rev. C **99**, 014613 (2019).

[25] V. Saiko and A. Karpov, Multinucleon transfer as a method for production of new heavy neutron-enriched isotopes of transuranium elements, Eur. Phys. J. A **58**, 41 (2022).

[26] Zhao-Qing Feng, Gen-Ming Jin, Jun-Qing Li, and Werner Scheid, Production of heavy and superheavy nuclei in massive fusion reactions, Nucl. Phys. A **816**, 33 (2009).

[27] Z.-Q. Feng, G.-M. Jin, and J.-Q. Li, Production of heavy isotopes in transfer reactions by collisions of $^{238}\mathrm{U}+^{238}\mathrm{U}$, Phys. Rev. C **80**, 067601 (2009).

[28] Z.-Q. Feng, Production of neutron–rich isotopes around $N=126$ in multinucleon transfer reactions, Phys. Rev. C **95**, 024615 (2017).

[29] K. Zhao, X. Wu, and Z. Li, Quantum molecular dynamics study of the mass distribution of products in 7.0A MeV $^{238}\mathrm{U}+^{238}\mathrm{U}$ collisions, Phys. Rev. C **80**, 054607 (2009).

[30] K. Zhao, Z. Li, Y. Zhang, N. Wang, Q. Li, C. Shen, Y. Wang, and X. Wu, Production of unknown neutron–rich isotopes in $^{238}\mathrm{U}+^{238}\mathrm{U}$ collisions at near-barrier energy, Phys. Rev. C **94**, 024601 (2016).

[31] N. Wang and L. Guo, New neutron-rich isotope production in $^{154}\mathrm{Sm}+^{160}\mathrm{Gd}$, Phys. Lett. B **760**, 236 (2016).

[32] C. Simenel, Nuclear quantum many-body dynamics, Eur. Phys. J. A **48**, 152 (2012).

[33] C. Simenel and A. S. Umar, Heavy-ion collisions and fission dynamics with the time–dependent Hartree-Fock theory and its extensions, Prog. Part. Nucl. Phys. **103**, 19 (2018).

[34] T. Nakatsukasa, K. Matsuyanagi, M. Matsuo, and K. Yabana, Time-dependent density-functional description of nuclear dynamics, Rev. Mod. Phys. **88**, 045004 (2016).

[35] V. E. Oberacker, A. S. Umar, and C. Simenel, Dissipative dynamics in quasifission, Phys. Rev. C **90**, 054605 (2014).

[36] A. S. Umar, V. E. Oberacker, and C. Simenel, Shape evolution and collective dynamics of quasifission in the time-dependent Hartree-Fock approach, Phys. Rev. C **92**, 024621 (2015).

[37] A. S. Umar and V. E. Oberacker, Time-dependent HF approach to SHE dynamics, Nucl. Phys. A **944**, 238 (2015).

[38] A. S. Umar, C. Simenel, and W. Ye, Transport properties of isospin asymmetric nuclear matter using the time-dependent Hartree–Fock method, Phys. Rev. C **96**, 024625 (2017).

[39] C. Simenel, Particle Transfer Reactions with the Time-Dependent Hartree-Fock Theory using a Particle Number Projection Technique, Phys. Rev. Lett. **105**, 192701 (2010).

[40] K. Sekizawa and K. Yabana, Time-dependent Hartree-Fock calculations for multinucleon transfer and quasifission processes in the $^{64}\mathrm{Ni}+^{238}\mathrm{U}$ reaction, Phys. Rev. C **93**, 054616 (2016).

[41] Kazuyuki Sekizawa, TDHF theory and its extensions for the multinucleon transfer reaction: A mini review, Front. Phys. **7**, 20 (2019).

[42] M. Tohyama and A. S. Umar, Quadrupole resonances in unstable oxygen isotopes in time-dependent density-matrix formalism, Phys. Lett. B **549**, 72 (2002).

[43] M. Tohyama, Applications of time-dependent density-matrix approach, Front. Phys. **8**, 67 (2020).

[44] C. Simenel, Particle-Number Fluctuations and Correlations in Transfer Reactions Obtained using the Balian-Vénéroni Variational Principle, Phys. Rev. Lett. **106**, 112502 (2011).

[45] D. Lacroix and S. Ayik, Stochastic quantum dynamics beyond mean field, Eur. Phys. J. A **50**, 95 (2014).

[46] R. Balian and M. Vénéroni, Time-dependent variational principle for the expectation value of an observable: Mean-field applications, Ann. Phys. (NY) **164**, 334 (1985).

[47] R. Balian and M. Vénéroni, Correlations and fluctuations in static and dynamic mean-field approaches, Ann. Phys. (NY) **216**, 351 (1992).

[48] E. Williams, K. Sekizawa, D. J. Hinde, C. Simenel, M. Dasgupta, I. P. Carter, K. J. Cook, D. Y. Jeung, S. D. McNeil, C. S. Palshetkar, D. C. Rafferty, K. Ramachandran, and A. Wakhle, Exploring Zeptosecond Quantum Equilibration Dynamics: From Deep-Inelastic to Fusion-Fission Outcomes in $^{58}\mathrm{Ni}+^{60}\mathrm{Ni}$ Reactions, Phys. Rev. Lett. **120**, 022501 (2018).

[49] K. Godbey and A. S. Umar, Quasifission dynamics in microscopic theories, Front. Phys. **8**, 40 (2020).

[50] K. Godbey, C. Simenel, and A. S. Umar, Microscopic predictions for the production of neutron-rich nuclei in the reaction $^{176}\mathrm{Yb}+^{176}\mathrm{Yb}$, Phys. Rev. C **101**, 034602 (2020).

[51] S. Ayik, A stochastic mean-field approach for nuclear dynamics, Phys. Lett. B **658**, 174 (2008).

[52] David J. Kedziora and Cédric Simenel, New inverse quasifission mechanism to produce neutron-rich transfermium nuclei, Phys. Rev. C **81**, 044613 (2010).

[53] A. S. Umar, M. R. Strayer, J. S. Wu, D. J. Dean, and M. C. Güçlü, Nuclear Hartree-Fock calculations with splines, Phys. Rev. C **44**, 2512 (1991).

[54] A. S. Umar and V. E. Oberacker, Three-dimensional unrestricted time-dependent Hartree-Fock fusion calculations using the full Skyrme interaction, Phys. Rev. C **73**, 054607 (2006).

[55] Ka–Hae Kim, Takaharu Otsuka, and Paul Bonche, Three-dimensional TDHF calculations for reactions of unstable nuclei, J. Phys. G: Nucl. Part. Phys. **23**, 1267 (1997).

[56] S. Ayik, B. Yilmaz, O. Yilmaz, A. S. Umar, and G. Turan, Multinucleon transfer in central collisions of $^{238}\mathrm{U}+^{238}\mathrm{U}$, Phys. Rev. C **96**, 024611 (2017).

[57] S. Ayik, B. Yilmaz, O. Yilmaz, and A. S. Umar, Quantal diffusion description of multinucleon transfers in heavy–ion collisions, Phys. Rev. C **97**, 054618 (2018).

[58] B. Yilmaz, S. Ayik, O. Yilmaz, and A. S. Umar, Multinucleon transfer in $^{58}\mathrm{Ni}+^{60}\mathrm{Ni}$ and $^{60}\mathrm{Ni}+^{60}\mathrm{Ni}$ in a stochastic mean-field approach, Phys. Rev. C **98**, 034604 (2018).

[59] S. Ayik, B. Yilmaz, O. Yilmaz, and A. S. Umar, Quantal diffusion approach for multinucleon transfers in Xe + Pb collisions, Phys. Rev. C **100**, 014609 (2019).

[60] S. Ayik, O. Yilmaz, B. Yilmaz, and A. S. Umar, Heavy-isotope production in $^{136}\mathrm{Xe}+^{208}\mathrm{Pb}$ collisions at $E_{\mathrm{c.m.}}=514$ MeV, Phys. Rev. C **100**, 044614 (2019).

[61] K. Sekizawa and S. Ayik, Quantal diffusion approach for multinucleon transfer processes in the ^{58,64}Ni + ^{208}Pb reactions: Toward the production of unknown neutron-rich nuclei, Phys. Rev. C **102**, 014620 (2020).

[62] S. Ayik and K. Sekizawa, Kinetic-energy dissipation and fluctuations in strongly damped heavy-ion collisions within the stochastic mean-field approach, Phys. Rev. C **102**, 064619 (2020).

[63] O. Yilmaz, G. Turan, and B. Yilmaz, Quasi-fission and fusion-fission reactions in ^{48}Ca + ^{208}Pb collisions at $E_{\text{c.m.}} = 190$ MeV, Eur. Phys. J. A **56**, 37 (2020).

[64] S. Ayik, M. Arik, E. C. Karanfil, O. Yilmaz, B. Yilmaz, and A. S. Umar, Quantal diffusion description of isotope production via the multinucleon transfer mechanism in ^{48}Ca + ^{238}U collisions, Phys. Rev. C **104**, 054614 (2021).

[65] C. W. Gardiner, *Quantum Noise* (Springer-Verlag, Berlin, 1991).

[66] U. Weiss, *Quantum Dissipative Systems*, 2nd ed. (World Scientific, Singapore, 1999).

[67] Hannes Risken and Till Frank, *The Fokker–Planck Equation* (Springer-Verlag, Berlin, 1996).

[68] A. C. Merchant and W. Nörenberg, Microscopic transport theory of heavy-ion collisions, Z. Phys. A **308**, 315 (1982).

[69] W. U. Schröder, J. R. Huizenga, and J. Randrup, Correlated mass and charge transport induced by statistical nucleon exchange in damped nuclear reactions, Phys. Lett. B **98**, 355 (1981).

[70] R. Charity, GEMINI: A code to simulate the decay of a compound nucleus by a series of binary decays, IAEA Technical Report No. INDC(NDS)-0530, 2008 (unpublished).